Influence of TCO and a-Si:H Doping on SHJ Contact Resistivity

Christoph Luderer, Leonard Tutsch, Christoph Messmer, Martin Hermle, and Martin Bivour

***Abstract*—Resistive losses in silicon heterojunction (SHJ) solar cells are partly linked to transport barriers at the amorphous silicon/crystalline silicon (a-Si:H/c-Si) and transparent conductive oxide (TCO)/a-Si:H interfaces. A key parameter is the position of the Fermi-level on either side of the junction which we modify by a systematic doping variation of the amorphous silicon and the transparent conductive oxide. We identify the charge carrier concentration to be the main driver for low contact resistance. For a-Si:H, this is achieved by using a sufficient but not too high doping gas concentration during deposition. For indium tin oxide (ITO) and aluminum zinc oxide (AZO), no or only a very low oxygen (O_2) gas concentration during deposition is needed. We show that a stack of low-oxygen ITO interlayer and an oxygen-rich ITO "bulk" layer is not only an effective means to combine efficient transport and low TCO absorption but also to improve the thermal stability of the a-Si:H/TCO/metal contact resistivity (ρ_c). Such a layer stack helps to relax the constraints regarding the optoelectrical performance and improves the efficiency of SHJ solar cells.**

***Index Terms*—Amorphous silicon, charge carrier concentration, contact resistivity, doping, series resistance, silicon heterojunction.**

I. Introduction

ENGINEERING amorphous silicon based heterojunction (SHJ) solar cells toward highly efficient and economic devices is governed by the pronounced trade-off between the optical and electrical properties of the nanometer thin amorphous silicon and transparent conductive oxide (TCO) films and their interfaces. Main limitations are the rather low short-circuit current density (J_{sc}) due to parasitic absorption of the amorphous silicon films and TCO [1] and significant resistive losses originating from high contact resistivities (ρ_c) in the stack of TCO/a-Si:H(n/p)/a-Si:H(i)/c-Si [2], [3]. ρ_c at the hole and electron contact are the main contributors to the series resistance (R_s) of SHJ cells [4], [5]. Resistive losses arise due to transport barriers at the critical junctions in the SHJ stack: the a-Si:H/c-Si and the TCO/a-Si:H junction [3]. The transport across these barriers takes place either via thermionic emission, if the barrier height is low enough, or via direct tunneling respectively trap-assisted tunneling (TAT) [6]–[8].

Especially on the TCO side, optical properties have to be considered while optimizing transport. However, electrical and optical properties are closely linked. A high carrier concentration, e.g., leads to a higher lateral conductivity [6] and a lower contact resistivity [9], [10] while reducing the transparency. Thus, high transparency has to be balanced with high conductivity, e.g., via tuning the TCO oxygen (O_2) content [11]. One way to relax the constraints on TCO optimization are high-mobility TCOs with $\mu_{\mathrm{TCO}} > 100\,\mathrm{cm}^2/\mathrm{Vs}$ allowing the reduction of the charge carrier concentration N_{TCO} for higher transparency while maintaining a high lateral conductivity [12]. Another option is to utilize layer stacks to decouple the required properties at the interface from the bulk layer [9], [13], [14].

In this contribution, we present a thorough investigation of vertical transport losses at the TCO/a-Si:H heterojunction. After a short discussion of the TCO/a-Si:H contact based on numerical device simulations, optimum a-Si:H doping for both electron and hole contact of our SHJ is investigated. Then, the TCO/a-Si:H contact resistance over a wide range of TCO resistivities (i.e., O_2 contents) for the a-Si:H(n) electron contact and a-Si:H(p) hole contact is examined. Indium tin oxide (ITO), the most commonly used TCO, is compared with aluminum zinc oxide (AZO), a potential candidate for SHJ cells with an indium-free TCO. Finally, the beneficial effect of an ITO stack on ρ_c and solar cell performance is presented.

II. Experimental

Resistance test structures for the electron (hole) contact were fabricated on random pyramid textured n-type (p-type) FZ silicon wafers. On the rear side, a doped a-Si:H layer capped with a stack of evaporated TiPdAg served as a low-ohmic rear contact. For the contacts to be investigated on the front side, stacks of intrinsic a-Si:H and doped a-Si:H have been deposited and contacted by a TCO and/or a stack of evaporated TiPdAg (Fig. 2c). More details can be found in [3]. Structures containing a-Si:H layers with different doping concentrations were fabricated via changing the dopant gas flow during plasma-enhanced chemical vapor deposition (PECVD). The total gas flow of pure hydrogen

Manuscript received September 21, 2020; revised November 27, 2020; accepted January 8, 2021. Date of publication January 29, 2021; date of current version February 19, 2021. This work was supported by the German Federal Ministry for Economic Affairs and Energy under Contract N° 03EE1032 "CUSTCO" within the SOLAR-ERA.Net program. *(Christoph Luderer and Leonard Tutsch are co-first authors.) (Corresponding author: Christoph Luderer.)*

Christoph Luderer, Leonard Tutsch, Martin Hermle, and Martin Bivour are with the Fraunhofer Institute for Solar Energy Systems, 79110 Freiburg, Germany (e-mail: christoph.luderer@ise.fraunhofer.de; leonard.tutsch@ise.fraunhofer.de; martin.hermle@ise.fraunhofer.de; martin.bivour@ise.fraunhofer.de).

Christoph Messmer is with the Fraunhofer Institute for Solar Energy Systems, 79110 Freiburg, Germany, and also with the Laboratory for Photovoltaic Energy Conversion Department of Sustainable Systems Engineering, University of Freiburg, 79110 Freiburg, Germany (e-mail: christoph.messmer@ise.fraunhofer.de).

Color versions of one or more figures in this article are available at https://doi.org/10.1109/JPHOTOV.2021.3051206.

Digital Object Identifier 10.1109/JPHOTOV.2021.3051206

This work is licensed under a Creative Commons Attribution 4.0 License. For more information, see https://creativecommons.org/licenses/by/4.0/

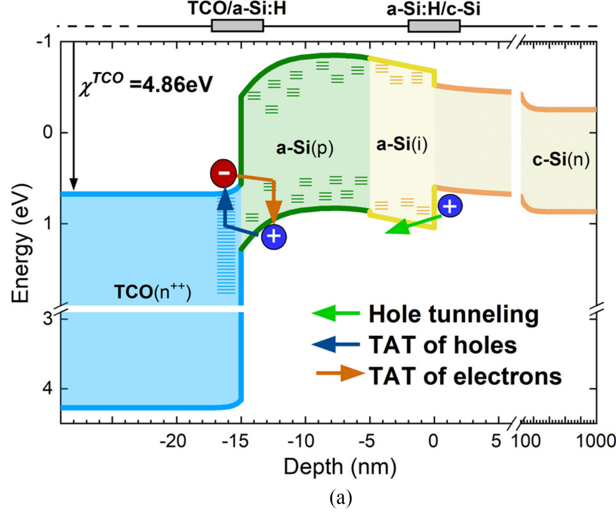

(a)

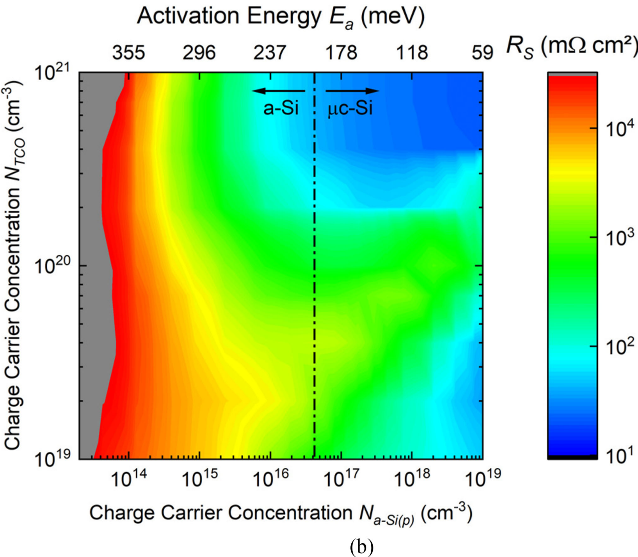

(b)

Fig. 1. (a) Band diagram of the SHJ hole contact at maximum power point. Important transport mechanisms are indicated (adapted from [17]). (b) Simulated R_s for SHJ solar cells as a function of doping in a-Si:H(p) and TCO at the hole contact.

and dopant gas diluted in hydrogen was fixed for all groups, as well as all other deposition parameters. The deposition time was adapted to reach a comparable layer thickness. For the ITO and AZO doping variation, the O_2 gas flow was varied during dc magnetron sputter deposition at ∼100 °C with target compositions of In_2O_3:SnO_2 (90:10 weight-%) and ZnO:Al_2O_3 (98:2 weight-%). The O_2 content in the sputtering gas, defined as the ratio of O_2 gas flow to the total gas flow, was in the range of 0% to 5.4% for ITO and between 0% and 1.2% for AZO. TCO layer properties were obtained from Hall effect measurements using the van der Pauw's method for films on glass substrates. Tungsten oxide (WO_x) layers were deposited by the evaporation of a stoichiometric WO_3 powder (>99.99% purity). Two-terminal dark-*I-V* measurements were performed on a WAVELABS Sinus-220 sun simulator to quantify the transport losses at the TCO/a-Si:H/c-Si heterojunction [3]. Subsequent consecutive thermal treatments were performed on a Präzitherm hotplate in air for 10 min each. Resistance values were extracted by means of curve fitting at zero voltage and c-Si bulk and rear contact contributions were subtracted from the total resistance to obtain ρ_c for the front contact. Corresponding 2×2 cm² solar cells were fabricated on random pyramid textured 200 μm thick 1 Ω·cm n-type c-Si wafers and received the same a-Si:H and TCO deposition parameters. Only the thickness of the doped a-Si:H layers was slightly thinner on cell level (14 nm) as compared to the resistance test structures (18 nm). The metallization of the cells was realized via screen printing of an Ag paste cured at 200 °C for 10 min in a belt furnace. All thicknesses indicated in this article are related to film thickness on planar substrate, and actual thicknesses on the textured substrate are expected to be lower by the geometric factor of ∼1.7.

III. Results & Discussion

A. Simulation of the TCO/a-Si:H(p) Contact

Fig. 1a shows a band diagram of the SHJ hole contact. Basically, low resistive hole extraction from the absorber toward the TCO is enabled by ensuring sufficiently high hole conductivity in all layers and at all interfaces along the transport paths [7], [15]. The total resistance is typically governed by the series connection of the 1) a-Si:H/c-Si and 2) TCO/a-Si:H contact resistance [3], as indicated in Fig. 1a. The influence of the a-Si:H and TCO doping on this total resistance is highlighted by the results from numerical device simulations shown in Fig. 1b. Fig. 1b shows a map of simulated R_s values as a function of the doping concentration in p-type a-Si:H and n-type TCO at the hole contact. The results were obtained with Sentaurus TCAD [16] based on the band diagram and the TAT paths depicted in Fig. 1a using simulation parameters as described in [17]. The electron contact was assumed to be ideal and lateral transport was not included in this one-dimensional simulation. Hence, for (almost) ideal behavior also at the hole contact, i.e. very low ρ_c, the wafer's resistivity is the only contributor to R_s (20 mΩ·cm², dark blue area). For a highly doped and therefore metal-like TCO ($N_{\mathrm{TCO}} > \sim 4.0 \times 10^{20}$ cm^{-3}), increasing the a-Si:H doping (*x*-axis) improves the contact to the absorber and to the TCO, as well as the transport through the a-Si:H "bulk." For TCOs with lower doping ($N_{\mathrm{TCO}} < \sim 2.0 \times 10^{20}$ cm^{-3}), which are typically used in solar cells due to higher transparency, higher resistance losses at the TCO/a-Si:H contact are responsible for the increase in R_s. For very low TCO doping, a positive influence due to better work function matching is predicted by the simulation (bottom right). While such an improved work function matching could be shown experimentally [14], [17], [18], no improved transport on device level was observed [14], [17].

Different tunneling scenarios have been discussed in detail already, e.g., in [7] and [8]. For the hole contact, band-to-band tunneling (B2BT) is possible across the TCO/a-Si:H(p) interface if the a-Si:H(p) valence band is properly aligned with the TCO conduction band. Band alignment can be reached with following two cases.

1) First, the activation energy E_a in a-Si:H(p) (top *x*-axis in Fig. 1b) has to be lower than the energy gap between TCO conduction band edge and Fermi energy [8], [14].

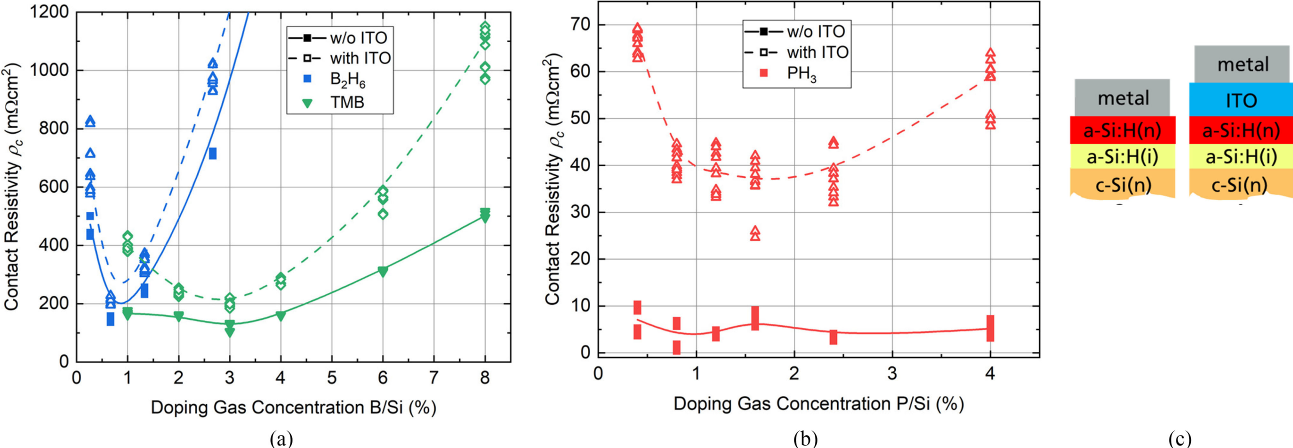

Fig. 2. Influence of doping gas concentration on the contact resistivity ρ_c for (a) the hole and (b) the electron contact after annealing at 180 °C. Dotted lines represent structures with ITO, solid lines structures without ITO. (c) Sketch of the different resistance test structures used for the electron contact. For the hole contact, boron-doped a-Si:H and c-Si bulk was used. The rear contact of all groups comprised only doped a-Si:H and full area metallization.

This would be fulfilled for very high N_{TCO} or very low E_a. The latter is difficult for a-Si:H(p) since E_a values below 200 meV cannot be reached in the amorphous state [19]. To reach lower E_a values, the deposition parameters have to be adapted to form micro- or nanocrystalline Si. Interestingly, the barrier height would be very high in this scenario but transport is efficient via B2BT (top right in Fig. 1b).

2) Second, for TCO work function to be higher than the a-Si:H(p) work function [20]. This case is also difficult to achieve with common ITO work functions reported in the range of 4.0–5.5 eV [18] and the a-Si:H valence band energy being at $E_{V,\mathrm{a\text{-}Si:H(p)}} = 5.62$ eV.

Failing proper band alignment, transport relies on trap states within the bandgap via capture and emission processes (TAT), as discussed in detail in [7] and [8]. The efficiency of TAT is given by the energetic position of the trap states relative to the Fermi level [8], [21]. Hence, it depends on doping with the general trend of high N_{TCO} and $N_{\mathrm{a\text{-}Si:H(p)}}$ being beneficial for transport.

B. a-Si:H Doping Variation

A low ρ_c at the TCO/a-Si:H and a-Si:H/c-Si heterojunctions can be reached by sufficient a-Si:H net doping [3], [9], [22]. The net doping of amorphous silicon is defined by the dopant concentration and the doping efficiency, which is reduced by defect creation [23]–[25]. Experimentally, the doping level can be controlled, among other deposition parameters, by the gas phase doping. In Fig. 2, ρ_c for the electron and hole contact after annealing at 180 °C is displayed for varying doping gas concentrations during deposition. The doping gas concentration is here defined as the ratio of dopant atoms B or P to Si atoms in the gas phase, thereby taking into account the number of dopant atoms per molecule. Samples with ITO (dotted lines) and without ITO (solid lines) between a-Si:H and the metal contact were fabricated, as depicted in Fig. 2c. The ITO O_2 content was 1.6% for all samples, corresponding to N_{TCO} of about 1.9×10^{20} cm^{-3} measured on glass after 180 °C annealing. For the hole contact in Fig. 2a, a distinctive optimum was observed for both doping gases under investigation. Using trimethylborane (TMB), optimum ρ_c was 150 mΩ·cm² without and 200 mΩ·cm² with ITO. Very similar results were obtained for diborane (B_2H_6, 160 mΩ·cm² without and 200 mΩ·cm² with ITO). In case of the same electrode material (either metal or ITO), ρ_c is expected to be lowest for a-Si:H with the highest charge carrier concentration $N_{\mathrm{a\text{-}Si:H(p)}}$, i.e., lowest E_a. The increase in ρ_c for lower doping gas concentrations can be explained by insufficient incorporation of dopants in the a-Si:H layer. In addition to the insufficiently induced c-Si band bending in the contact region, transport through the a-Si:H "bulk" is deteriorated with lower active dopant concentration and lower density of states within the a-Si:H bandgap. An increased ρ_c was also observed for doping concentrations above the optimum. In this process region, dopants are available in abundance. The defect density increases significantly with rising doping concentration [23]–[26]; therefore, a decreasing $N_{\mathrm{a\text{-}Si:H(p)}}$ can also be assumed in this region.

Adding ITO to the structure increased ρ_c for all doping concentrations. That ITO increases ρ_c of the SHJ stack was discussed previously [3]. Interestingly, the increase due to ITO was not constant for the different doping concentrations. Using TMB for example, at minimum ρ_c, the increase in ρ_c due to ITO was 50 mΩ·cm², whereas it was 200 mΩ·cm² for the lowest and even 500 mΩ·cm² for the highest doping concentration. This shows that $N_{\mathrm{a\text{-}Si:H(p)}}$ influences both the a-Si:H/c-Si and the TCO/a-Si:H contact significantly.

These trends were also observed for the electron contact (Fig. 2b). Without ITO, ρ_c values below 10 mΩ·cm² were reached. Such low values are prone to errors, as discussed in [3]. With ITO electrode, the optimum for the electron contact was less distinct compared to the hole contact. Similar ρ_c values were reached in the doping gas concentration range between 0.8% and 2.4% with lowest $\rho_c = 25$ mΩ·cm² at 1.6%. Optimum doping concentrations of TMB and PH_3 were used for further investigations in the following sections.

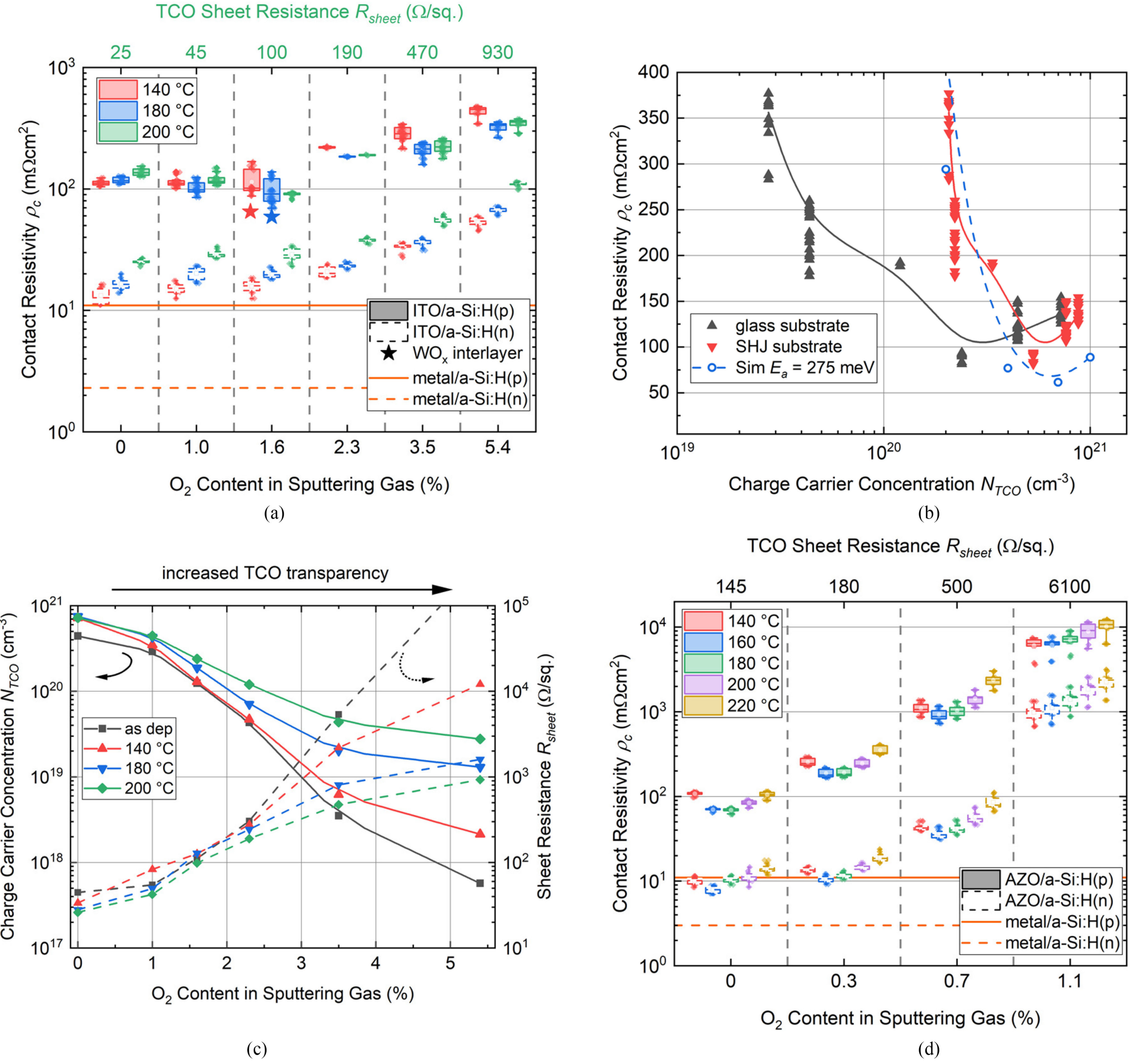

Fig. 3. Influence of the TCO O_2 content and annealing on ρ_c and TCO layer properties. (a) ITO/a-Si:H(n) and ITO/a-Si:H(p) contact resistivity. R_{sheet} values on the top x-axis were measured after 200 °C annealing. (b) ρ_c for the hole contact plotted against N_{ITO} measured on glass or SHJ substrate after 200 °C annealing. For comparison, simulated data with E_a fixed at 275 meV was added. (c) N_{TCO} and R_{sheet} for ITO as measured on glass. (d) AZO contacts on a-Si:H(p) and a-Si:H(n). R_{sheet} values on the top x-axis were measured as sputtered. The intrinsic a-Si:H layer was omitted in the resistance test structures to be more sensitive to the TCO/a-Si:H contact. As a reference, metal/a-Si:H ρ_c is indicated by horizontal lines in (a) and (d).

C. TCO Doping (O_2 Content) Variation, AZO and ITO

Fig. 3c shows N_{TCO} and sheet resistance (R_{sheet}) of ∼105 nm ITO measured on glass as a function of O_2 content in the sputtering gas. Rising O_2 content decreased N_{TCO} on glass by three orders of magnitude in the as deposited state. Annealing in air at different temperatures steadily increased N_{TCO} for all ITO layers. This increase is more apparent for O_2-rich ITOs with lower initial N_{TCO}. The same trend was observed by Haschke *et al*. for two ITO layers with different O_2 content [27]. Similarly, R_{sheet} increased with rising O_2 content and decreased for all groups during annealing. Hall effect parameters are highly dependent on the used substrate, i.e., planar glass or H_2-rich a-Si:H on a random pyramid textured c-Si wafer [28]–[30]. Nevertheless, the same qualitative trends seen on glass were also observed for N_{TCO} and R_{sheet} obtained from Hall effect measurements on textured SHJ precursor (not shown). AZO was more sensitive to small changes in O_2 content. This led to the scattering of Hall parameters from run to run (not shown). Nevertheless, on average, N_{TCO} decreased similarly to ITO with increased O_2 content in the sputtering gas from 3.1×10^{20} cm^{-3} at 0% to 6.0×10^{19} cm^{-3} at 1.2% O_2 in the sputtering gas.

As discussed above and addressed in [10] and [14], low ρ_c at the TCO/doped a-Si:H interface results from efficient tunneling

rather than efficient work function matching. Assuming that the a-Si:H is sufficiently doped, efficient tunneling can be achieved if the TCO provides a metal-like behavior, i.e., the TCO is degenerately doped and if the interface is free of resistive interlayers [17]. Experimentally, depositing TCO with low O_2 content in the sputtering gas facilitates both. The influence of the O_2 content on ρ_c for both ITO and AZO on n- and p-type a-Si:H is depicted in Fig. 3. The different colors indicate the influence of the post-deposition annealing temperature. As a reference, ρ_c of the metal/a-Si:H contact annealed at 180 °C are indicated with horizontal lines. Please note that unlike for the investigations of the a-Si:H doping, the intrinsic a-Si:H layer was omitted in these resistance test structures to be more sensitive to the TCO/a-Si:H contact.

In the case of ITO, at the electron contact, ρ_c decreased monotonically with decreasing O_2 content (Fig. 3a). In the range of 0–2.3%, which results in R_{sheet} values typically applied in SHJ cells, ρ_c increased only slightly and is almost constant on a very low level for a-Si:H(n). Similarly, ρ_c for the hole contact increased with rising O_2 content (Fig. 3a). Lowest ρ_c values for ITO deposited with a medium O_2 content of 1.6% indicate an optimum for this process. However, this is close to the wafer-to-wafer scattering. It is obvious that even for highest N_{TCO}, the TCO/a-Si:H contact is inferior compared to the metal/a-Si:H contact.

In Fig. 3b, ρ_c for the hole contact is plotted against N_{TCO} measured on glass and on a textured SHJ precursor after 200 °C annealing. On SHJ substrate, higher N_{TCO} were obtained, but please note that absolute N_{TCO} values on different substrates cannot be compared, as mentioned above [28]–[30]. The experimentally obtained trend coincides with the simulated R_s for $E_a = 275$ meV. Please note that the contributions of the wafer (20 mΩ·cm²) and the intrinsic layer ($\sim$150 mΩ·cm² [3]) were subtracted from simulated R_s, thereby making it comparable to the experimental ρ_c data. The slight increase in resistance for the hole contact at highest N_{TCO} approaching 1.0×10^{21} cm^{-3} observed experimentally is also predicted by the simulation for E_a above 220 meV. This could be explained by an increased work function mismatch due to a too low ITO work function. When the a-Si:H activation energy was below 220 meV, this trend was not observed. Most likely because tunneling is more efficient and the increased work function mismatch is irrelevant in that case.

Below $N_{\mathrm{TCO}} = 2.0 \times 10^{20}$ cm^{-3}, ρ_c was increased monotonically with decreasing N_{TCO} (increasing ITO work function). Thus, the reduction of the transport barrier height due to increased ITO work function is not large enough to be beneficial for ρ_c, since it is (over)compensated by less efficient tunneling due to lower N_{TCO}. A material with higher work function than low-oxygen ITO is needed for proper band alignment with a-Si:H(p). Indeed, ρ_c for the hole contact could be reduced with a 10 nm layer of high work function tungsten oxide (WO_x) at the TCO/a-Si:H(p) interface (stars in Fig. 3a). WO_x work functions up to 6.7 eV have been achieved [31], depending on the composition of the oxide [32]–[34]. It has to be mentioned, however, that the effective work function at the junction depends highly on the interface properties like the defect density (Fermi-level pinning) [35], [36]. In [37], it was shown that a WO_x interlayer at the hole contact can improve the fill factor (*FF*) of SHJ cells.

AZO contacts (Fig. 3d) showed similar to ITO increasing resistance with increasing O_2 content independent of the a-Si:H doping, whereas the contact resistance for the hole contact is about one order of magnitude higher than for the electron contact. On p-type a-Si:H, optimum ρ_c values for lowest AZO O_2 content were below optimum ρ_c values for ITO. With introducing additional O_2 to the sputtering plasma during deposition, ρ_c increased steeply by two orders of magnitude.

As indicated by the different colors, the resistance of the metal/TCO/a-Si:H stack changed upon annealing in ambient air with an optimum between 140 °C and 180 °C depending on the TCO O_2 content and the a-Si:H doping polarity. For AZO, the same trends were observed as for ITO. At 200 °C, a temperature commonly used to cure screen-printed Ag pastes for SHJ solar cells, the resistance already degraded for all investigated structures. Possible reasons for the degradation of ρ_c would be decreased N_{TCO} in ITO or increased E_a in a-Si:H. However, Fig. 3c shows that N_{TCO} on glass rather increased during annealing in this temperature range. Note that ITO used for Hall effect measurements was uncapped and in direct contact with air during annealing unlike the resistance test structures. This might influence the TCO modification during annealing, as will be shown in the next section. For structures without ITO or intrinsic a-Si:H, no degradation of ρ_c was observed [3]. Therefore, it is most likely that changes directly at the TCO/a-Si:H interface are responsible for the increased ρ_c for both electron and hole contact. Feasible from thermodynamic considerations [38], [39] is the formation, thickening, or densification of silicon oxide at the TCO/a-Si:H interface during annealing with oxygen from the TCO [14], [17], [40], [41]. In-depth structural analysis of the TCO/a-Si:H interface and its changes due to annealing would be necessary for a definitive explanation.

TCO sheet resistances displayed at the top *x*-axis were measured on glass after 200 °C annealing for ITO and in the as deposited state for AZO. It can be seen in Fig. 3b and c that Hall parameters change upon annealing and depend on the used substrate. For that reason, displayed TCO sheet resistance values are only meant to show the relevance of the particular TCO for device integration.

D. TCO Layer Stack: Lower and More Temperature Stable ρ_c

In the previous section, it was shown that highly transparent O_2-rich TCOs suffer from high ρ_c (in addition to high R_{sheet}). Fig. 4a displays again the ρ_c of medium-O_2 ITO (1.6%, group 1) in comparison to ρ_c of O_2-rich ITO (3.5%, group 2). To improve ρ_c of the O_2-rich ITO without adding much parasitic absorption a 20 nm thin, highly conductive ITO interlayer (1.0% O_2) was introduced either at the ITO/a-Si:H (group 3) or ITO/metal interface (group 4). In both cases, the total resistance could be reduced compared to the reference structure without any ITO interlayer. The interlayer at the ITO/a-Si:H interface seems to be more effective, as slightly lower ρ_c values were obtained compared to the structure with the interlayer at the ITO/metal interface. With the ITO interlayer at the a-Si:H interface, similar

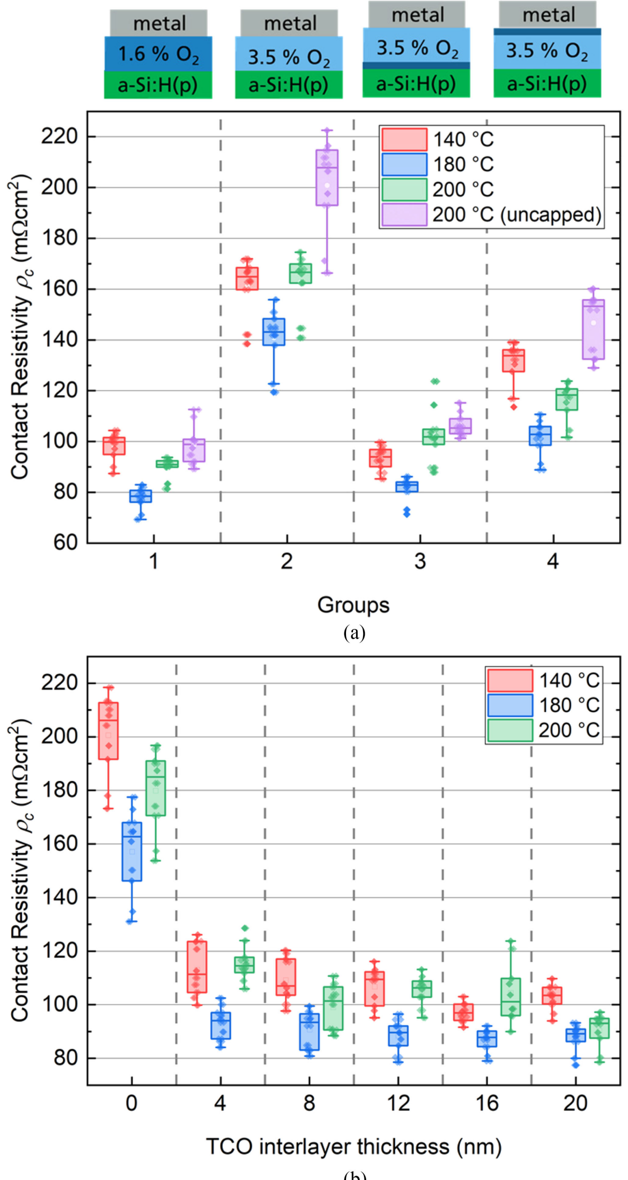

Fig. 4. (a) Contact resistivity (ρ_c) measurements of different ITO/a-Si:H(p) heterojunction stacks. The samples consisted of a metal/ITO/boron doped a-Si:H stack at the front (as depicted above) and a low-ohmic rear contact. (b) ρ_c as a function of the ITO interlayer thickness at the a-Si:H interface. The intrinsic a-Si:H layer was omitted in (a) and (b) to be more sensitive to the TCO/a-Si:H contact.

ρ_c as for 1.6%-O_2 ITO (group 1) was obtained. The reason for the lower overall resistance with such interlayer could be an improved contact at the interfaces due to higher N_{TCO}. Another reason could be a less pronounced formation of resistive oxides [17] due to less excess oxygen at the ITO/Si interface.

For our resistance test structures, as for other structures commonly used to extract ρ_c of SHJ (TLM, Cox and Strack), the TCO was capped by metal during the annealing. In solar cells, however, only a small fraction of the TCO is capped by the metal grid, leaving most of the TCO in direct contact with ambient air during curing/sintering of the metal paste after screen printing. In an attempt to account for that, the annealing of resistance test structures was performed prior to the front side metallization, i.e., the ITO layer was uncapped during annealing in air. Red, blue, and green data in Fig. 4a were obtained from samples consecutively annealed at different temperatures after metallization. Violet data result from samples that were exposed to the same temperature treatments but prior to metallization at the front. Note that these samples received an additional annealing at 180 °C after metallization to ensure no influence from uncured metallization at the front. The rear side for all samples was metallized prior to annealing to ensure low-ohmic behavior. For medium-O_2 ITO (1.6% O_2, group 1), no significant difference in resistance was observed between the capped and uncapped annealing. Therefore, it seems legitimate to use our standard approach of annealing structures capped with metal to quantify resistive losses of heterojunction stacks containing low- to medium-O_2 ITOs. However, for oxygen-rich ITO (3.5% O_2, group 2), a higher resistance was observed for uncapped ITO compared to capped ITO. It should be noted that very similar resistances were obtained with twice the ITO thickness (not shown here). Therefore, it can be concluded that changes at the interfaces rather than vertical transport via the TCO bulk seem to dominate ρ_c. Possible could be a stronger interaction of O_2-rich ITO with oxygen from the air compared to low- or medium-O_2 ITO. For example, in [42], it was shown for IO:H that the higher the O_2 content during deposition, the larger the difference in N_{TCO} of films annealed in air or in vacuum was.

With an ITO interlayer at the metal interface (group 4), annealing prior to the metallization (ITO uncapped) still lead to increased ρ_c. With the ITO interlayer at the a-Si:H interface, however, ρ_c was independent of the annealing method. It is worth mentioning that these trends were also observed on a-Si:H(n) (not shown here). This indicates that the ITO/a-Si:H interface is not only limiting regarding the overall ρ_c, but also most sensitive to (chemical) modification during annealing resulting in higher contact resistance.

A thickness variation of the oxygen-poor ITO interlayer was conducted to check the minimum thickness needed to benefit from the improved contact properties (Fig. 4b). The total ITO thickness of the stack was fixed to 105 nm. Even for the thinnest interlayer of only 4 nm (effective thickness on textured surface even lower), a reduction by about 50 mΩ·cm² (almost) down to the level of $\rho_{c,\ 1.6\%\ \mathrm{ITO}}$ was observed. With increasing interlayer thickness, ρ_c hardly changed. Thus, ρ_c can be considered rather independent of the interlayer thickness. If efficient homogenization of both ITOs during annealing occurs, one would expect to obtain lower ρ_c the higher the share of low-oxygen ITO is in the stack, i.e., with increasing interlayer thickness. However, this is not the case, indicating that the O_2 content respectively N_{TCO} directly at or in the immediate vicinity of the ITO/a-Si:H interface dominates the transport behavior. The weak thickness dependence could also point toward the avoidance of an O_2-rich layer at the ITO/a-Si:H interface by using O_2-poor sputtering gas during the initial TCO growth.

As a result, O_2-rich ITO can be used as "bulk" ITO to form an overall highly transparent layer, while the ultra-thin interlayer prevents the deterioration of ρ_c. Similarly, in [9], ρ_c was found rather independent of the O_2 content within the "bulk" ITO with a 15 nm thick low-oxygen interlayer. Instead of O_2-rich

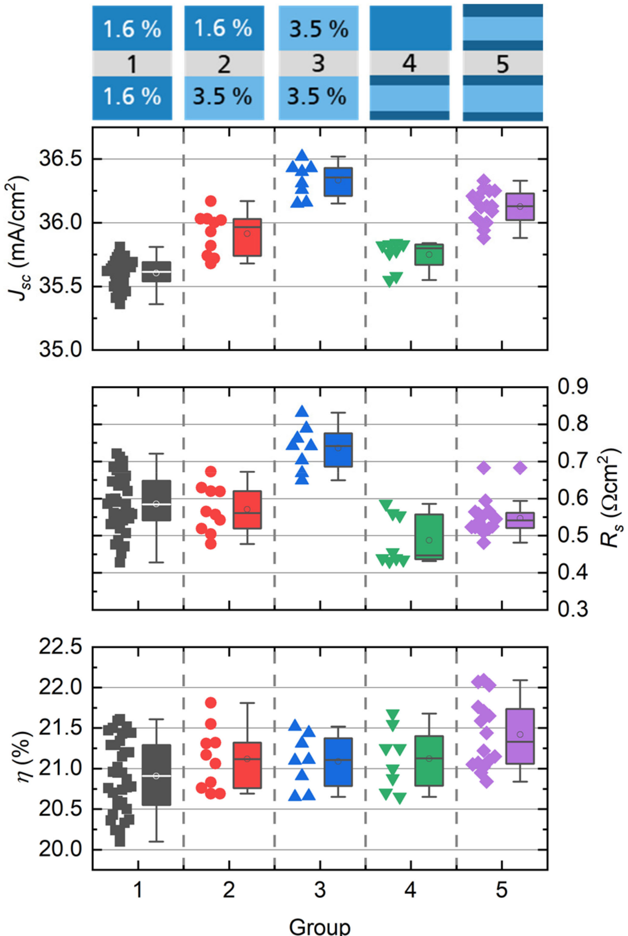

Fig. 5. *J–V* parameters of different SHJ solar cells in the rear emitter design. The sketched structure for each group is depicted at the top.

ITO also other even more transparent materials like SiN_x, SiO_x, or TiO_x could be used as anti-reflection coating replacing the O_2-rich "bulk" TCO with the additional benefit of less indium consumption [43]–[45].

E. SHJ Solar Cells With ITO Stack

In solar cells, optical and electrical properties have to be balanced to achieve high J_{sc} and low R_s. Regarding R_s not only ρ_c but also sufficient lateral transport (low R_{sheet}) has to be considered. J_{sc} and R_s as well as the power conversion efficiency (η) of fabricated monofacial n-type SHJ solar cells in rear emitter design (hole contact at the rear side) are shown in Fig. 5. Please note that the cell performance is limited by the low J_{sc} due to a simplistic grid design with a busbar shading of 4% of the total cell area. Reference group 1 represents cells with our standard ITO process of 1.6% O_2 on both front and rear side. A gain in J_{sc} was observed using oxygen-rich ITO (3.5% O_2) only on the rear side (group 2) and an even more pronounced J_{sc} gain was observed when oxygen-rich ITO was used on both sides (group 3). However, R_s increased accordingly due to increased ρ_c and sheet resistance for oxygen-rich ITO, as depicted in Fig. 3. To combine high transparency with low ρ_c and to ensure only moderate chemical modification of the TCO/a-Si:H interface during curing of the screen-printed metal paste at 200 °C, the oxygen-rich ITO was deposited in between two low-oxygen ITO interlayer (1.0% O_2, 20 nm thickness) on the rear side (group 4) or on both sides (group 5). Especially for group 5, a clear gain in J_{sc} was achieved compared to reference group 1, whereas the R_s was in the same range for both groups. This shows that in addition to ρ_c also R_{sheet} was sufficiently low using O_2-rich ITO in combination with low-oxygen ITO interlayer. It is important to mention that lateral transport is not only provided by the TCO, but also by the silicon absorber [46]. The distribution of lateral transport between absorber and TCO is determined by ρ_c and efficient coupling is only possibly with low ρ_c. Therefore, the reduction of ρ_c is not only important for vertical but also for lateral transport. The passivation quality was not influenced by the TCO variation. Pseudo fill factor (p*FF*) was 83.1 ± 1.1% and open-circuit voltage (V_{oc}) was 730 ± 3 mV for all groups. Hence, group 5 exhibits to a maximum η of 22.1% which is significantly higher compared to the cells using single TCO layers. The use of even thinner interlayers well below 20 nm is expected to provide even better optics and consequently further improved η.

IV. Conclusion

The influence of a-Si:H and TCO doping on the transport losses at the electron and hole contact of SHJ cells was investigated. For a-Si:H, there is an optimum doping gas concentration regarding ρ_c (3% for TMB, 0.8% for B_2H_6, and 1.6% for PH_3). For both investigated TCOs, AZO and ITO, ρ_c increased with increasing O_2 content and showed lower tolerance to annealing, independently of the a-Si:H doping polarity. However, overall higher ρ_c were obtained for the hole contact compared to the electron contact throughout all TCO variations. ρ_c of contacts including AZO can be as low as or even lower than ρ_c of standard ITO/a-Si:H contacts if optimum conditions are used, i.e., no O_2 added to the sputtering gas during AZO deposition. Furthermore, it was shown that ρ_c can strongly depend on the thermal budget of the post-deposition treatment and on whether or not the TCO was capped with metal during this treatment.

It could also be shown that the trade-off between optical and electrical TCO properties can be relaxed using a low-O_2 ITO interlayer at the ITO/a-Si:H interface in combination with O_2-rich "bulk" ITO. The use of such a TCO stack leads to an improved power conversion efficiency on cell level.

Acknowledgment

The authors would like to thank A. Leimenstoll, F. Schätzle, and K. Zimmermann for sample preparation, D. Kurt and Z. Newcomb-Hall for sample preparation and dark *I–V* measurements, and F. Martin for measuring the solar cells.

References

[1] Z. C. Holman *et al.*, "Current losses at the front of silicon heterojunction solar cells," *IEEE J. Photovolt.*, vol. 2, no. 1, pp. 7–15, Jan. 2012.

[2] T. F. Schulze, L. Korte, E. Conrad, M. Schmidt, and B. Rech, "Electrical transport mechanisms in a-Si: H/c-Si heterojunction solar cells," *J. Appl. Phys.*, vol. 107, no. 2, pp. 23711–23713, 2010.

[3] C. Luderer, C. Messmer, M. Hermle, and M. Bivour, "Transport losses at the TCO/a-Si:H/c-Si heterojunction: Influence of different layers and annealing," *IEEE J. Photovolt.*, vol. 10, no. 4, pp. 1–7, Jul. 2020.

[4] L. Basset, W. Favre, D. Munoz, and J. P. Vilcot, "Series resistance breakdown of silicon heterojunction solar cells produced on CEA-INES pilot line," in *Proc. 35th Eur. Photovolt. Sol. Energy Conf. Exhib.*, 2018, pp. 721–724.

[5] D. Lachenal *et al.*, "Heterojunction and passivated contacts: A simple method to extract both n/TCO and p/TCO contacts resistivity," *Energy Procedia*, vol. 92, pp. 932–938, 2016.

[6] S. Kirner *et al.*, "The influence of ITO dopant density on J-V characteristics of silicon heterojunction solar cells: Experiments and simulations," *Energy Procedia*, vol. 77, pp. 725–732, 2015.

[7] C. Messmer, M. Bivour, J. Schön, and M. Hermle, "Requirements for efficient hole extraction in transition metal oxide-based silicon heterojunction solar cells," *J. Appl. Phys.*, vol. 124, no. 8, 2018, Art. no. 85702.

[8] P. Procel *et al.*, "The role of heterointerfaces and subgap energy states on transport mechanisms in silicon heterojunction solar cells," *Prog. Photovolt. Res. Appl.*, vol. 28, no. 9, pp. 935–945, 2020.

[9] M. Leilaeioun *et al.*, "Contact resistivity of the p-Type amorphous silicon hole contact in silicon heterojunction solar cells," *IEEE J. Photovolt.*, vol. 10, no. 1, pp. 54–62, Jan. 2020.

[10] P. Procel, G. Yang, O. Isabella, and M. Zeman, "Theoretical evaluation of contact stack for high efficiency IBC-SHJ solar cells," *Sol. Energy Mater. Sol. Cells*, vol. 186, pp. 66–77, 2018.

[11] B. G. Lewis and D. C. Paine, "Applications and processing of transparent conducting oxides," *MRS Bulletin*, vol. 25, no. 8, pp. 22–27, 2000.

[12] T. Koida, H. Fujiwara, and M. Kondo, "Hydrogen-doped In_2O_3 as High-mobility transparent conductive oxide," *Jpn. J. Appl. Phys.*, vol. 46, no. 28, pp. L685–L687, 2007.

[13] L. Barraud *et al.*, "Hydrogen-doped indium oxide/indium tin oxide bilayers for high-efficiency silicon heterojunction solar cells," *Sol. Energy Mater. Sol. Cells*, vol. 115, pp. 151–156, 2013.

[14] M. Bivour, *Silicon Heterojunction Solar Cells: Analysis and Basic Understanding*. Stuttgart, Germany: Fraunhofer Verlag, 2015.

[15] U. Würfel, A. Cuevas, and P. Würfel, "Charge carrier separation in solar cells," *IEEE J. Photovolt.*, vol. 5, no. 1, pp. 461–469, Jan. 2015.

[16] Synopsis. (2019). *Sentaurus TCAD: Release Q-2019.12*. [Online]. Available: http://www.synopsys.com

[17] C. Messmer *et al.*, "Influence of interfacial oxides at TCO/Doped Si thin film contacts on the charge carrier transport of passivating contacts," *IEEE J. Photovolt.*, vol. 10, no. 2, pp. 343–350, Mar. 2020.

[18] A. Klein *et al.*, "Transparent conducting oxides for photovoltaics: Manipulation of Fermi level, work function and energy band alignment," *Materials*, vol. 3, no. 11, pp. 4892–4914, 2010.

[19] W. E. Spear and P. G. Le Comber, "Substitutional doping of amorphous silicon," *Solid State Commun.*, vol. 17, no. 9, pp. 1193–1196, 1975.

[20] M. Bivour, S. Schröer, and M. Hermle, "Numerical analysis of electrical TCO / a-Si:H(p) contact properties for silicon heterojunction solar cells," *Energy Procedia*, vol. 38, pp. 658–669, 2013.

[21] W. Goes *et al.*, "Identification of oxide defects in semiconductor devices: A systematic approach linking DFT to rate equations and experimental evidence," *Microelectron. Rel.*, vol. 87, pp. 286–320, 2018.

[22] G. Nogay *et al.*, "Nanocrystalline silicon carrier collectors for silicon heterojunction solar cells and impact on low-temperature device characteristics," *IEEE J. Photovolt.*, vol. 6, no. 6, pp. 1654–1662, Nov. 2016.

[23] M. Stutzmann, D. K. Biegelsen, and R. A. Street, "Detailed investigation of doping in hydrogenated amorphous silicon and germanium," *Phys. Rev. B*, vol. 35, no. 11, pp. 5666–5701, 1987.

[24] R. A. Street, "Localized states in doped amorphous silicon," *J. Non-Cryst. Solids*, vol. pp. 77–78, pp. 1–16, 1985.

[25] L. Korte, E. Conrad, H. Angermann, R. Stangl, and M. Schmidt, "Advances in a-Si:H/c-Si heterojunction solar cell fabrication and characterization," *Sol. Energy Mater. Sol. Cells*, vol. 93, no. 6–7, pp. 905–910, 2009.

[26] D. Pysch, C. Meinhard, N.-P. Harder, M. Hermle, and S. W. Glunz, "Analysis and optimization approach for the doped amorphous layers of silicon heterojunction solar cells," *J. Appl. Phys.*, vol. 110, no. 9, 2011, Art. no. 94516.

[27] J. Haschke *et al.*, "Annealing of silicon heterojunction solar cells: Interplay of solar cell and indium tin oxide properties: Interplay of solar cell and ITO properties," *IEEE J. Photovolt.*, vol. 9, no. 5, pp. 1202–1207, Sep. 2019.

[28] K.-U. Ritzau, T. Behrendt, D. Palaferri, M. Bivour, and M. Hermle, "Hydrogen doping of indium tin oxide due to thermal treatment of heterojunction solar cells," *Thin Solid Films*, vol. 599, pp. 161–165, 2016.

[29] A. Cruz *et al.*, "Influence of silicon layers on the growth of ITO and AZO in silicon heterojunction solar cells," *IEEE J. Photovolt.*, vol. 10, no. 2, pp. 703–709, Mar. 2020.

[30] D. Erfurt *et al.*, "Impact of rough substrates on hydrogen-doped indium oxides for the application in CIGS devices," *Sol. Energy Mater. Sol. Cells*, vol. 206, 2020, Art. no. 110300.

[31] J. Meyer *et al.*, "Charge generation layers comprising transition metal-oxide/organic interfaces: Electronic structure and charge generation mechanism," *Appl. Phys. Lett.*, vol. 96, no. 19, 2010, Art. no. 193302.

[32] D. Menzel, M. Mews, B. Rech, and L. Korte, "Electronic structure of indium-tungsten-oxide alloys and their energy band alignment at the heterojunction to crystalline silicon," *Appl. Phys. Lett.*, vol. 112, no. 1, 2018, Art. no. 11602.

[33] M. Mews, L. Korte, and B. Rech, "Oxygen vacancies in tungsten oxide and their influence on tungsten oxide/silicon heterojunction solar cells," *Sol. Energy Mater. Sol. Cells*, vol. 158, pp. 77–83, 2016.

[34] M. Vasilopoulou *et al.*, "Reduction of tungsten oxide: A path towards dual functionality utilization for efficient anode and cathode interfacial layers in organic light-emitting diodes," *Adv. Funct. Mater.*, vol. 21, no. 8, pp. 1489–1497, 2011.

[35] A. Dimoulas, P. Tsipas, A. Sotiropoulos, and E. K. Evangelou, "Fermi-level pinning and charge neutrality level in germanium," *Appl. Phys. Lett.*, vol. 89, no. 25, 2006, Art. no. 252110.

[36] A. Agrawal *et al.*, "Fermi level depinning and contact resistivity reduction using a reduced titania interlayer in n-silicon metal-insulator-semiconductor ohmic contacts," *Appl. Phys. Lett.*, vol. 104, no. 11, 2014, Art. no. 112101.

[37] M. Bivour, J. Temmler, H. Steinkemper, and M. Hermle, "Molybdenum and tungsten oxide: High work function wide band gap contact materials for hole selective contacts of silicon solar cells," *Sol. Energy Mater. Sol. Cells*, vol. 142, pp. 34–41, 2015.

[38] L. G. Gerling, C. Voz, R. Alcubilla, and J. Puigdollers, "Origin of passivation in hole-selective transition metal oxides for crystalline silicon heterojunction solar cells," *J. Mater. Res.*, vol. 32, no. 2, pp. 260–268, 2017.

[39] M. T. Greiner, L. Chai, M. G. Helander, W.-M. Tang, and Z.-H. Lu, "Metal/Metal-oxide interfaces: How metal contacts affect the work function and band structure of MoO_3," *Adv. Funct. Mater.*, vol. 23, no. 2, pp. 215–226, 2013.

[40] M. Wimmer *et al.*, "Hard x-ray photoelectron spectroscopy study of the buried Si/ZnO thin-film solar cell interface: Direct evidence for the formation of Si–O at the expense of Zn-O bonds," *Appl. Phys. Lett.*, vol. 99, no. 15, 2011, Art. no. 152104.

[41] L. Tutsch *et al.*, "Implementing transparent conducting oxides by DC sputtering on ultrathin SiOx / poly-Si passivating contacts," *Sol. Energy Mater. Sol. Cells*, vol. 200, 2019, Art. no. 109960.

[42] D. Erfurt *et al.*, "Improved electrical properties of pulsed DC magnetron sputtered hydrogen doped indium oxide after annealing in air," *Mater. Sci. Semicond. Process.*, vol. 89, pp. 170–175, 2019.

[43] S. Y. Herasimenka, W. J. Dauksher, M. Boccard, and S. Bowden, "ITO/SiOx:H stacks for silicon heterojunction solar cells," *Sol. Energy Mater. Sol. Cells*, vol. 158, pp. 98–101, 2016.

[44] D. L. Bätzner *et al.*, "'HJT 2.0' performance improvements and cost benefits for silicon heterojuntion cell production," in *Proc. 36th Eur. Photovolt. Sol. Energy Conf. Exhib.*, 2019.

[45] A. B. Morales-Vilches *et al.*, "ITO-Free silicon heterojunction solar cells with ZnO:Al/SiO 2 front electrodes reaching a conversion efficiency of 23%," *IEEE J. Photovolt.*, vol. 9, no. 1, pp. 34–39, Jan. 2019.

[46] J. Haschke *et al.*, "Lateral transport in silicon solar cells," *J. Appl. Phys.*, vol. 127, no. 11, 2020, Art. no. 114501.